

Modeling Coupled Evaporation and Seepage in Ventilated Tunnels

T. A. Ghezzehei^{*}, R. C. Trautz, S. Finsterle, P. J. Cook, and C. F. Ahlers¹

Earth Sciences Division
Lawrence Berkeley National Laboratory
University of California
MS 90R1116, 1 Cyclotron Rd.,
Berkeley, CA 94720-8126

Manuscript submitted to
Vadose Zone Journal (TOUGH special issue)

^{*} Corresponding author, Tel (510) 486-5688, Fax (510) 486-5686, Email TAGhezzehei@lbl.gov

¹ Now at *LFR Levine Fricke, Costa Mesa, California*

ABSTRACT

1
2 Tunnels excavated in unsaturated geological formations are important to activities such
3 as nuclear waste disposal and mining. Such tunnels provide a unique setting for simultaneous
4 occurrence of seepage and evaporation. Previously, inverse numerical modeling of field liquid-
5 release tests and associated seepage into tunnels were used to provide seepage-related large-scale
6 formation properties by ignoring the impact of evaporation. The applicability of such models was
7 limited to the narrow range of ventilation conditions under which the models were calibrated.
8 The objective of this study was to alleviate this limitation by incorporating evaporation into the
9 seepage models. We modeled evaporation as an isothermal vapor diffusion process. The semi-
10 physical model accounts for the relative humidity, temperature, and ventilation conditions of the
11 tunnels. The evaporation boundary layer thickness (BLT) over which diffusion occurs was
12 estimated by calibration against free-water evaporation data collected inside the experimental
13 tunnels. The estimated values of BLT were 5 to 7 mm for the open underground tunnels and 20
14 mm for niches closed off by bulkheads. Compared to previous models that neglected the effect of
15 evaporation, this new approach showed significant improvement in capturing seepage
16 fluctuations into open tunnels of low relative humidity. At high relative- humidity values, the
17 effect of evaporation on seepage was very small.

18

INTRODUCTION

18
19 Seepage of liquid water into tunnels is an important phenomenon for subsurface activities
20 such as mining and geologic disposal of nuclear wastes. A key factor affecting the long-term
21 safety of the proposed nuclear waste repository at Yucca Mountain (YM), Nevada, is the seepage
22 of liquid water into waste emplacement tunnels. The rate, chemical composition, and spatial and
23 temporal distributions of seepage are critical factors that determine corrosion of waste canisters,
24 integrity of engineered barriers, and dissolution and mobilization of contaminants and their
25 release to groundwater (Bodvarsson et al., 1999; Finsterle et al., 2003). In unsaturated
26 formations, capillary forces hold the pore water tightly in the formation and prevent it from
27 seeping by gravitational forces into the tunnel – the invisible barrier created by the capillary
28 force is commonly known as a “capillary barrier.” Philip and co-workers (Knight et al., 1989;
29 Philip, 1989a; Philip, 1989b; Philip et al., 1989a; Philip et al., 1989b) considered steady-state
30 unsaturated flow around capillary barriers and provided analytical solutions for the critical
31 conditions that trigger seepage into various idealized tunnel geometries excavated in
32 homogeneous formations. Detailed numerical models have been used to study unsaturated flow
33 in heterogeneous fractured media and seepage into tunnels of various geometries under transient
34 conditions (e.g., Birkholzer et al., 1999; Finsterle, 2000; Finsterle and Trautz, 2001; Li and
35 Tsang, 2003). Site-specific seepage models for the nuclear waste repository at Yucca Mountain,
36 Nevada were developed by calibrating the effective seepage-related parameters against field
37 seepage test data (Finsterle et al., 2003).

38 Most of the previous numerical models assumed that liquid water leaking into a tunnel
39 drips (seeps) immediately at the place of entry. The potential for evaporation to compete with
40 seepage has been generally ignored, and its effect was lumped with the effective flow parameters

64 area of the ambient air. Accurate modeling of these coupled processes is difficult for several
65 reasons: (1) the first step is a non isothermal phenomenon, and the parameters that govern this
66 process are strongly temperature dependent; (2) the vapor concentration gradient in the boundary
67 layer is strongly influenced by the air flow regime; and (3) the air flow depends on among other
68 things the ambient wind velocity and the roughness of the evaporating surface.

69 Ho (1997) and Or and Ghezzehei (2000) modeled evaporation from individual water
70 droplets attached to tunnel ceilings, assuming constant temperature and humidity conditions.
71 However, the scale of their approach is too small to be incorporated into the larger scale seepage
72 models that represent the discrete dripping process as a continuum flow. Therefore, the
73 evaporation model required in this study should be of an intermediate scale and be compatible
74 with the existing seepage models. The formulation used herein capitalizes on the observed
75 dependence of evaporation rate on tunnel humidity and ventilation conditions, and the
76 availability of high resolution time-series data of relative humidity, temperature and free-water
77 evaporation rate (Trautz and Wang, 2002).

78 In the following subsections, we introduce an isothermal vapor diffusion model of
79 evaporation and define the problem domain and boundary conditions. This is followed by
80 estimation of the evaporation model parameters, using free-water evaporation data. Finally, a
81 remark on evaporation from porous surface is provided.

82 **Isothermal Vapor Diffusion Model**

83 To simplify the first step of evaporation (vaporization) we assume the following: (1) the
84 absorption of latent heat and its effect on the physical properties of the liquid-vapor interface are
85 ignored; (2) the time dependence of the vaporization process (e.g., Zhang and Wang, 2002;
86 Zhang et al., 2001) is neglected; and (3) the vapor partial pressure of the interfacial air is

87 assumed to be under thermodynamic equilibrium. At equilibrium, the air above a flat surface of
 88 pure water is considered saturated with vapor; its vapor pressure is denoted by p_s . This
 89 saturation vapor pressure rises with temperature. In the temperature range of -10°C to 50°C , the
 90 saturation vapor pressure is related to interfacial temperature by (Murray, 1966):

$$91 \quad \ln p_s = a \frac{T}{T+b} + c \quad [1]$$

92 where $a = 21.87$, $b = 265.5^{\circ}\text{C}$ and $c = 6.41$ are constants, and T is the interfacial temperature.
 93 For non-flat interfaces (such as capillary menisci) the actual interfacial vapor pressure p is
 94 related to the interfacial capillary potential by the classic Kelvin equation,

$$95 \quad \ln \left(\frac{p}{p_s} \right) = P_C \cdot \frac{M_W}{\rho_W R T} \quad [2]$$

96 where P_C is the capillary pressure, ρ_W and M_W are the density and molecular mass of liquid
 97 water, respectively, and R is the universal gas constant. Note that the relative humidity of air is
 98 defined as the ratio of the actual partial pressure (p) to the saturated vapor pressure (p_s)

$$99 \quad h = p/p_s \quad [3]$$

100 The second step of evaporation, vapor removal from the interface, is modeled as a first-
 101 order phenomena described by Fickian diffusion (Rohsenow and Choi, 1961). In one dimension
 102 and under constant temperature, the vapor flux (J_v) is given by

$$103 \quad J_v|_T = -D_v \cdot \frac{dC}{dz} \quad [4]$$

104 where D_v is the vapor diffusion coefficient, which is related to the ambient air pressure (P) and
 105 air temperature (T) by

106
$$D_V = 2.13 \times 10^{-5} \frac{10^5}{P} \left(\frac{T}{273.15} \right)^{1.8} \quad [5]$$

107 and the vapor concentration C is related to vapor pressure by

108
$$C = \frac{M_W}{RT} \cdot p \quad [6]$$

109 In the subsequent subsection, we define the problem domain and develop the appropriate
110 boundary conditions needed to solve the vapor diffusion equation [4].

111 **Velocity and Concentration Boundary Layers**

112 In admitting diffusive flux as the primary mechanism for vapor removal from the
113 evaporating surface, we tacitly assume that airflow above the evaporating surface is fully
114 developed and laminar, as illustrated in Fig. 1a. The free-stream air velocity (V^∞) is retarded in
115 the vicinity of the evaporating surface because of frictional resistance. The air velocity parallel to
116 the evaporating surface increases from $V = 0$ at $z = 0$ (no-slip) asymptotically to $V = V^\infty$ at a
117 distance sufficiently far away from the surface. For fully laminar flow conditions, the thickness
118 of the boundary layer of retarded velocity (defined as $V \leq 0.99V^\infty$) is inversely proportional to
119 the square root of the free-stream velocity (Rohsenow and Choi, 1961):

120
$$\delta_V \propto 1/\sqrt{V^\infty} \quad [7]$$

121 Because the equations that describe laminar air flow parallel to a flat surface and
122 diffusion from a flat surface are analogous (Rohsenow and Choi, 1961), a similar notion of
123 concentration boundary layer holds near the evaporating surface. The vapor concentration profile
124 is illustrated in Fig. 1b. The vapor concentration decreases from an equilibrium value ($C = C^0$) at
125 $z = 0$ to a value determined by the free-stream humidity at sufficiently far distance. The

126 concentration boundary layer thickness (δ_C) is related to the velocity boundary layer thickness
 127 by the Schmidt number,

$$128 \quad Sc = \frac{\delta_C}{\delta_V} = \frac{\mu_a}{\rho_a \cdot D} \quad [8]$$

129 where μ_a and ρ_a are the viscosity and density of air, respectively. At 20 °C and 1 atm pressure,
 130 the Schmidt number is approximately unity. In the remainder of this paper the subscripts in the
 131 boundary layer thickness are dropped and $\delta = \delta_V = \delta_C$. It is evident from [7] and [8] that the
 132 concentration BLT (δ) is inversely related to the square root of the free-stream velocity (V^∞)
 133 and can serve as a direct measure of the tunnel ventilation condition. In a subsequent subsection,
 134 estimation of the BLT will provide further elaboration on the dependence of δ on ventilation
 135 conditions.

136 Fig. 1. Schematic description of (a) air velocity and (b) vapor concentration profiles above a
 137 free water surface

138 **Boundary Conditions**

139 The domain of the vapor diffusion equation [4] is the concentration boundary layer
 140 introduced in the preceding subsection. The boundary condition on [4] corresponding to the
 141 equilibrium vapor concentration at the evaporating surface ($z = 0$) is given by (using [2] and
 142 [6]):

$$143 \quad C = C^0 = \frac{M_W}{R T} p_s \exp \left[\frac{P_C}{\rho_W} \frac{M_W}{R T} \right] \quad [9]$$

144 The second boundary condition is at the border of the concentration boundary layer $z = \delta$, where
 145 the vapor concentration is defined by the relative humidity (h) of the ambient air:

146
$$C = C^\infty = \frac{M_W}{R T} p_s h \quad [10]$$

147 If the boundary conditions change slowly, the evaporation rate can be considered to be at
148 steady state and the concentration gradient $\mathbf{d}C/\mathbf{d}z$ is constant throughout the boundary layer.
149 Then, the steady state vapor diffusion equation [4] under isothermal conditions is simplified to

150
$$J_V = -D_v \cdot \frac{C^0 - C^\infty}{\delta} \quad [11]$$

151 Note that the ratio δ/D_v is commonly referred to as aerodynamic resistance. The isothermal
152 vapor diffusion equation [11] is considered valid for modeling evaporation from tunnel surfaces
153 and free water. Fujimaki and Inoue (2003) found [11] (also known as the bulk transfer equation)
154 to be valid in laboratory evaporation experiments in which the ambient air velocity was on the
155 order of 1 m/s. All the variables of this model are directly related to physical conditions in the
156 tunnel, and all of them, except δ , can be independently determined from measured quantities.
157 The boundary-layer thickness (δ) can be estimated by calibrating [11] against free water
158 evaporation data, as discussed in the next subsection.

159 **Estimation of the Boundary-Layer Thickness**

160 Apart from the capillary pressure at the evaporating surface, evaporation from free water
161 and that from a wet porous surface are thus far assumed to be identical processes. Therefore, a
162 controlled evaporation experiment from a still water surface can be used to estimate the vapor
163 concentration boundary layer thickness, which is also applicable to evaporation from wet tunnel
164 surfaces at similar ventilation conditions. Upon substitution of [1], [5], [9], and [10] in [11], and
165 noting that the capillary pressure of the free water surface is $P_C = 0$, we arrive at a free-water
166 evaporation equation,

$$J_V = -2.13 \times 10^{-5} \frac{10^5}{P} \left(\frac{T}{273.15} \right)^{1.8} \cdot \left(a \frac{T}{T+b} + c \right) \cdot \frac{M_w}{RT} \frac{1-h}{\delta} \quad [12]$$

167
168 According to the isothermal assumption, T denotes the temperature of the evaporating surface
169 and the surrounding air. Assuming the change in conditions that affect evaporation rate is slow
170 compared to the time it takes to reach steady-state evaporation, [12] can be fitted to time-series
171 data of evaporation rate data, measured at known temperature, pressure, and relative humidity
172 conditions. The best-fit δ represents the boundary-layer thickness at the prevailing ventilation
173 condition. However, it should also be noted that uncertainties associated with the assumed
174 simplifications (including isothermal conditions, flat evaporating surface, and laminar airflow)
175 are lumped in this parameter. Thus, the boundary-layer thickness should be considered an
176 effective parameter.

177 **Evaporation from Porous Surface**

178 The surface of an unsaturated porous medium typically consists of solid (matrix of the
179 medium) and pore/fracture (liquid and gas) components, rendering the evaporating surface
180 heterogeneous with respect to vapor concentration, as illustrated in Fig. 2a. During seepage,
181 however, tunnel ceilings are usually covered with liquid films (e.g., Trautz and Wang, 2001), and
182 the vapor concentration could be considered locally homogeneous. For simplicity, we extend
183 this assumption of locally uniform distribution of vapor concentration to the entire tunnel Fig.
184 2b. The vapor concentration at any given location on the tunnel is assumed to be at capillary
185 equilibrium with the pores and fractures of the porous medium. The datum $z = 0$ for the vapor
186 diffusion is set on the surface of the tunnel (as illustrated in Fig. 2b). Although this assumption is
187 likely to fail at very low saturations (when the liquid is scattered in a few fine pores and

188 fractures) it is expected to be of marginal consequence because the evaporation rate under such
189 conditions is very low.

190 Fig. 2. Evaporating surface area of a porous medium: (a) partitioning of the surface into non-
191 evaporating solid and evaporating pores; (b) proposed approach of uniform gas-phase
192 surface. The dark shade denotes vapor in pores and/or fractures.

193 **COUPLED SEEPAGE AND EVAPORATION**

194 In a tunnel constructed in unsaturated formations, the flow velocity of water in the rock is
195 usually stagnated near the crown, resulting in elevated moisture (Philip et al., 1989b). Unlike
196 evaporation from ground surface, where infiltration opposes the evaporation flux, the condition
197 in tunnels is favorable for simultaneous occurrence of evaporation and seepage. Field tests that
198 exhibit simultaneous evaporation and seepage are described below. After field test descriptions,
199 we present a brief description of seepage modeling using the numerical simulators TOUGH2
200 (Pruess et al., 1999) and iTOUGH2 (Finsterle, 1999) and discuss implementation of evaporation
201 in these models.

202 **Field Tests**

203 The data reported in this paper were obtained from field tests and measurements
204 conducted at the proposed nuclear waste repository at Yucca Mountain currently under
205 investigation by the US Department of Energy (DOE). Air-injection tests were conducted to
206 characterize the permeability and small-scale heterogeneities of the formation, and liquid-release
207 tests were performed to study seepage phenomena. Relative humidity, temperature, and free-
208 water evaporation were monitored at the test site to assess the evaporation conditions. Detailed
209 description of the site and tests conducted at the site are provided elsewhere (Birkholzer et al.,

210 1999; Bodvarsson et al., 1999; Finsterle and Trautz, 2001; Finsterle et al., 2003; Trautz and
211 Wang, 2001; Trautz and Wang, 2002; Wang et al., 1999). This study is concerned with the lower
212 lithophysal welded tuff unit at Yucca Mountain, in which about 80% of the proposed repository
213 is expected to reside. This unit contains many small fractures (less than 1 m long) and is
214 interspersed with numerous lithophysal cavities (0.15 m–1 m in diameter).

215 In the lower lithophysal unit, an 800-m long drift (5 m in diameter) for enhanced
216 characterization of the repository block (ECRB) was excavated off the main Exploratory Studies
217 Facility (ESF) tunnel. Liquid-release and air-injection tests were systematically conducted in this
218 ECRB Cross Drift along boreholes drilled into the ceiling of the Cross Drift at regular intervals.
219 Similar tests were conducted in a short (approximately 15 m long) drift excavated off the Cross
220 Drift (niches). Schematic alignment of the tunnels is shown in Fig. 3a. This paper is concerned
221 with tests conducted at a Cross Drift borehole designated as LA#2 (Fig. 3b) and a short drift
222 known as Niche 5 (Fig. 3c). The tests and measurements conducted in the Cross Drift and Niche
223 5 are briefly described below.

224 **Air-injection tests**

225 The purpose of the air-injection tests was to estimate absolute permeability of the
226 formation as a basis for the stochastic generation of heterogeneous permeability fields. Short
227 sections of the boreholes (0.3 m in Niche 5, 1.8 m in Cross Drift) were isolated using an
228 inflatable packer system, and compressed air was injected. Air injection was terminated when
229 steady-state pressure was reached. Air-permeability values were derived from the steady-state
230 pressure data according to an analytical solution of LeCain (1995). Permeabilities determined
231 from air-injection tests were considered representative of the absolute permeability of the test
232 interval.

233 **Liquid-release Tests**

234 Liquid release tests were conducted in boreholes drilled above tunnels to evaluate
235 seepage into waste emplacement drifts. The alignment of the boreholes and test intervals are
236 schematically shown in Fig. 3. The liquid release boreholes in the Cross Drift were
237 approximately 20 m long, drilled into the ceiling of the Cross Drift at a nominal inclination of
238 15° from the horizontal. Liquid release data from a borehole designated as LA#2 were used in
239 this study. The borehole was partitioned into three zones (designated as Zone 1, Zone 2, and
240 Zone 3) available for liquid release testing. The distances from the middle of the liquid-release
241 zones to the drift crown were 1.58 m, 2.84 m, and 4.10 m for Zone 1, Zone 2, and Zone 3,
242 respectively. The liquid release boreholes in Niche 5 were near horizontal. Of the six boreholes
243 available for tests, data from boreholes #4 and #5 were used in this study. The liquid release tests
244 were performed by injecting water into a test interval isolated by inflated rubber packers. Water
245 that seeped into the tunnels was captured and measured using automated recording devices.

246 **Relative Humidity and Temperature Measurements**

247 The Cross Drift was actively ventilated during regular working hours, thus the relative
248 humidity of the tunnel was usually low. To mitigate the effect of evaporation in the seepage
249 process, the seepage collection interval was guarded using curtains on both ends. Because Niche
250 5 was isolated from the actively ventilated Cross Drift by a bulkhead, the relative humidity was
251 relatively high. To aid in the estimation of evaporation during the liquid release tests, the relative
252 humidity and temperature of the air inside and outside of the curtains (for the Cross Drift) and in
253 front of and behind the bulkhead (for Niche 5) were monitored.

254 The evaporation rate from still water was measured by monitoring the level (mass) of
 255 water in evaporation pans placed within the space enclosed by the seepage capture tray and end
 256 curtains (for the Cross Drift tests) and behind the bulkhead (for Niche 5).

257 Fig. 3. Schematic alignment of tunnels and boreholes: (a) parts of the Exploratory Studies
 258 Facility (ESF) tunnel and Enhanced Characterization of the Repository Block (ECRB)
 259 cross-drift; (b) liquid release test setup in the Cross Drift, including liquid release
 260 intervals and liquid injection and seepage collection equipment; and (c) vertical section
 261 of Niche 5 along with location of all the test boreholes.

262 **TOUGH2/iTOUGH2 Seepage Model**

263 A detailed description of the numerical models developed for flow in fractured formation
 264 around a tunnel and associated seepage into the tunnel using TOUGH2/iTOUGH is given by
 265 Finsterle et al (2003). A summary follows.

266 The TOUGH2 code is an integral finite difference simulator that represents unsaturated
 267 flow at the scale of individual grids by Richards' equation (Bear, 1972; Pruess et al., 1999)

$$268 \quad \phi \rho \frac{\partial}{\partial t} S_e = \text{div} \left[k \frac{\rho}{\mu} \nabla (P_C + \rho g z) \right] \quad [13]$$

269 The appropriateness of using this continuum approach to simulate water flow through
 270 unsaturated fractured rock was shown by Finsterle (2000). The effective permeability (k) and
 271 capillary pressure (P_C) are functions of liquid saturation as given by van Genuchten's models
 272 (1980)

$$273 \quad k = k_a S_e^{1/2} \left[1 - \left(1 - S_e^{1/m} \right)^m \right]^2 \quad [14]$$

$$P_C = -\frac{1}{\alpha} \left[S_e^{-1/m} - 1 \right]^{1-m} \quad [15]$$

274 where k_a is the absolute permeability, $1/\alpha$ and m are fitting parameters with $\alpha > 0$ and
 275 $0 < m < 1$, and the effective saturation, S_e , is defined as $S_e = (S - S_{lr}) / (1 - S_{lr})$, with S_{lr} being the
 276 residual liquid saturation. While the k_a values were considered spatially heterogeneous, the $1/\alpha$,
 277 m , and S_{lr} parameters were summed to be homogeneous for a given test bed (Finsterle et al.,
 278 2003). The absolute permeability, k_a , was derived from the air-injection tests. The van
 279 Genuchten m parameter and the residual saturation were taken to be $m = 0.608$ and $S_{lr} = 0.01$,
 280 respectively (Finsterle et al., 2003). The van Genuchten capillary strength parameter $1/\alpha$ was
 281 estimated through inverse modeling. In the numerical seepage model, the condition for seepage
 282 is determined by the total water-potential gradient at the connection between the porous medium
 283 and the tunnel, as depicted in Fig. 4. The flow rate along the connection between the porous
 284 medium and the tunnel is given by

$$q_z = k \frac{\rho}{\mu} \frac{\Delta P + \rho g z}{\Delta z} \quad [16]$$

287 where ΔP denotes the capillary pressure difference across the distance between the last
 288 formation node and the tunnel node Δz . The nodal distance Δz is chosen to be a representative
 289 of the average length of fractures intersecting the tunnel that are not draining laterally (Finsterle
 290 et al., 2003). From [16], and assuming that the capillary pressure in the opening is zero, it
 291 follows that downward seepage ($q_z > 0$) occurs only when the following condition is satisfied:

$$-P_C^* > \rho g \Delta z \quad [17]$$

292 where P_C^* is the threshold capillary pressure at the last node adjacent to the opening. The critical
 293 capillary pressure $P_C^* = -\rho g \Delta z$ depends on the grid size or nodal distance of the numerical

295 model. According to [17], the tunnel surface does not need to be fully saturated for seepage to
 296 commence as in the case of unfractured homogeneous porous media (Philip et al., 1989b).

297 Fig. 4. Schematic description of the seepage and evaporation connections between nodes that
 298 represent the rock of the tunnel wall and the tunnel.

299 Implementation of Evaporation in TOUGH2

300 While seepage occurs only when the critical condition given in [17] is satisfied, vapor
 301 flow from/to tunnel walls to/from tunnel air occurs as long as there is vapor pressure
 302 disequilibrium between them. Coupling of the seepage and evaporation processes is illustrated in
 303 Fig. 4. Mass-transfer rate of water, including seepage, is represented in TOUGH2 by equations
 304 similar to [16], where the driving force is pressure gradient. To incorporate evaporation into the
 305 existing model without significant changes to the governing flow equations, we must rewrite the
 306 concentration-gradient dependent diffusion equation [11] in the form of equation [16]. Noting
 307 that the connection length Δz denotes the vapor concentration boundary layer thickness δ , the
 308 equivalent evaporative permeability can be written as

$$309 \quad k_{eq} = D_v \frac{\mu}{\rho} \left(\frac{C^0 - C^\infty}{P_C^0 - P_C^\infty} \right) \quad [18]$$

310 where the variables with a superscript of 0 correspond to the tunnel wall and those with a
 311 superscript of ∞ denote the tunnel air. The capillary pressure of the tunnel P_C^∞ is equivalent to
 312 the relative humidity [3] of the tunnel, as described by Kelvin's equation [2]. The vapor
 313 concentrations are computed according to [11] and [12]. Equation [18] was implemented in
 314 TOUGH2 as a special evaporation connection. When the conditions for both evaporation and

315 seepage permit, the total mass flow from the tunnel wall to the tunnel is considered as the sum of
316 both.

317 **Numerical Meshes**

318 Different numerical models were constructed to simulate liquid-release tests and seepage
319 into the underground openings at different test locations. Three-dimensional meshes of the test
320 sites were generated with grid sizes of $0.3 \text{ m} \times 0.1 \text{ m} \times 0.1 \text{ m}$ for the Cross Drift and $0.1 \text{ m} \times$
321 $0.1 \text{ m} \times 0.1 \text{ m}$ for Niche 5 (see Fig. 5). For the Cross Drift meshes, a circular cylindrical tunnel
322 of 5 m diameter was removed from the center of the mesh to represent the tunnel. Only one half
323 of the symmetric mesh was used in the simulations to save computational load. For the Niche 5
324 meshes, surveyed niche geometry was removed from the numerical mesh to replicate the test
325 sites. The liquid-release boreholes are indicated in Fig. 5 by bold black lines, and the white
326 sections at the middle of the boreholes represent the injection intervals. The Cross Drift borehole
327 is inclined while the Niche 5 boreholes are parallel to the centerline of the niche. The Cross Drift
328 mesh in Fig. 5a represents the Zone 2 test interval. In Fig. 5b and Fig. 5c, boreholes #4 and #5
329 are revealed, respectively (see also Fig. 3c). Notice that the injection intervals in boreholes #4
330 and #5 are located at 3–3.5 m and 8.5–8.8 m, respectively, from the borehole collars; hence, the
331 respective tunnel outlines are different.

332 Fig. 5. Numerical meshes of (a) Niche 5 with borehole #4, (b) Niche 5 with borehole #5, and
333 (c) the Cross Drift, along with a typical realization of the correlated stochastic
334 permeability field. Bold black lines denote the liquid-release boreholes, and the white
335 section in the middle of the boreholes is the injection interval.

336 The spatial structure of the Niche 5 permeability data was analyzed using the GSLIB
 337 module GAMV3 (Deutsch and Journel, 1992) and a spherical semivariogram was fitted to the
 338 resulting variogram. Because only six permeability data were available from the Cross Drift,
 339 assumed spherical variogram parameters were used. Recall that the permeability of the Cross
 340 Drift was measured on 1.8 m long intervals of the boreholes, and the standard deviation of the
 341 measured data was 0.21. The variability of the permeability on the scale of the 0.3 m long
 342 gridblock was expected to be greater than the measurement interval. For the purpose of
 343 generating a heterogeneous field, the permeability was taken to be log-normally distributed with
 344 a variance (sill) value of 1 order of magnitude. Computed and prescribed geostatistical
 345 parameters (Table 1) were used to generate spatially correlated permeability fields, using the
 346 sequential indicator simulation (SISIM) module of the GSLIB (Deutsch and Journel, 1992).
 347 Multiple realizations of the permeability field were generated and mapped to the numerical
 348 meshes. Representative permeability field realizations for the Cross Drift and Niche 5 are shown
 349 in Fig. 5.

350 Table 1. Mean, standard deviation, and correlation length of log-permeability data collected in
 351 the Cross Drift and Niche 5. The values in parentheses are prescribed values because the
 352 number of measurements was not adequate to compute the respective parameters.

Location	<i>n</i>	Mean log (k) [m ²]	Std. Dev. [m ²]	Spherical Variogram		
				Sill Value [log(k) ²]	Correlation length [m]	Nugget effect [log(k) ²]
Niche 5	61	-10.95	1.31	1.81	0.91	0.02
Cross Drift	6	-10.73	0.21	1.0	0.2	-

353

354 The tunnels were represented in the seepage models by two types of overlapping
355 gridblocks, one corresponding to seepage and the other to evaporation. The seepage gridblocks
356 were assigned a zero capillary pressure, whereas the evaporation gridblocks were assigned a
357 capillary pressure and vapor concentration corresponding to the tunnel relative humidity of the
358 tunnel, as given by [2] and [3]. No-flow boundary conditions are specified at the left, right, front,
359 and back sides of the model. A free-drainage boundary condition is applied at the bottom to
360 prevent an unphysical capillary boundary effect.

361 RESULTS AND DISCUSSIONS

362 Evaporation Boundary Layer

363 The evaporation data collected in Niche 5 were used to calibrate the evaporation model.
364 The data were grouped into three classes based on airflow velocity (ventilation): (1) inside Niche
365 5 without ventilation; (2) outside Niche 5 with active ventilation; and (3) outside Niche 5 without
366 active ventilation, the regime usually encountered during nights and weekends. In Fig. 6, the
367 measured relative humidity, and temperature, and evaporation rates from still water are plotted.
368 The evaporation model [12] was fitted to the measured data by adjusting the boundary layer
369 thickness. The best-fit estimates of the boundary layer thickness are listed in Table 2.

370 Fig. 6. Temperature, humidity, and evaporation rate data, along with model fit of the
371 evaporation data for inside and outside of Niche 5.

372 In agreement with the theoretical assessment (Equation [7]), the estimated δ showed an
373 inverse relationship with the ventilation conditions. Inside Niche 5, the air was the calmest
374 because it was isolated from the Cross Drift by a bulkhead (see Fig. 3). As a result, the thickest
375 boundary layer (20 mm) was obtained inside Niche 5. Fig. 6 shows that the relative humidity

376 outside Niche 5 increases at nights and during weekends when active tunnel ventilation is turned
 377 off. However, this increase in relative humidity is insufficient to explain the observed decrease in
 378 evaporation. Therefore, as shown in Fig. 6, reduced air ventilation during nights and weekends is
 379 also accompanied by an increase in the thickness of the boundary layer. The estimated boundary-
 380 layer-thickness values and Equation [7] suggest that the air velocity outside Niche 5 is higher
 381 than the inside by factors of 7 (without active ventilation) and 16 (with active ventilation). These
 382 results confirm the applicability of Equation [12] to describe the effects of humidity,
 383 temperature, and ventilation on evaporation rate.

384 Table 2. Summary of estimated boundary layer thickness for Niche 5 and their application.

Location of Experiment	δ (mm)	Used For Simulation of Liquid-Release Tests in
Inside Niche 5	20.0	Niche 5
Outside Niche 5, ventilation off	7.5	Cross Drift (with end curtains)
Outside Niche 5, ventilation on	5.0	Not used

385

386 **Coupled Seepage and Evaporation**

387 In this section, simulations of coupled seepage and evaporation are compared with
 388 measured seepage rate data. The software iTOUGH2 (Finsterle, 1999) was used to match the
 389 simulated seepage rate with the measured values by adjusting the free capillary strength
 390 parameter ($1/\alpha$) (Finsterle et al., 2003). The corresponding evaporation rate from the tunnel
 391 walls simulated using the tunnel relative humidity and calibrated boundary layer thickness.

392 **Niche 5**

393 Here, two different data sets from liquid release tests conducted in boreholes #4 (October,
394 2002) and #5 (July 2002) are compared with the Niche 5 seepage models. The liquid release rate,
395 seepage rate, and relative humidity data as well as modeled liquid release rate and fitted seepage
396 rate are shown in Fig. 7. The best-fit $1/\alpha$ values were 671 ± 223 Pa and 740 ± 339 Pa for
397 boreholes #4 (30 inversions) and #5 (24 inversions), respectively. The measured seepage rates
398 attained a steady-state flow rate after several days. Because the early-time transient data are
399 biased by storage (e.g., in lithophysal cavities and matrix) and/or fast flow paths connecting the
400 injection interval to the tunnel ceilings, the model was fitted to the late-time steady state data. In
401 the simulations, the relative humidity was kept constant at 0.85 to match with the lowest steady-
402 conditions observed during the borehole #4 tests.

403 Fig. 7. Calibration of seepage-rate data from liquid-release tests conducted in Niche 5.

404 Calculated seepage rate curves show only one of the multiple inversions.

405 To quantify the impact of evaporation on seepage over the observed high relative
406 humidity range (0.85–0.99), the calibrated seepage model of borehole #4 was used to simulate
407 seepage and evaporation at relative humidity values of 0.85, 0.95, and 0.99. The resulting steady
408 state seepage and evaporation rates (on Day 10) are plotted as percentages of the liquid release
409 rate in Fig. 8. At a relative humidity of 0.85, the evaporation rate from the entire niche wall
410 surface and the seepage rate are comparable in magnitude. As the relative humidity was
411 increased, the steady-state evaporation rate showed a drastic decrease, while the corresponding
412 seepage rate increased only slightly. Thus, at these high relative humidity conditions, the main
413 impact of evaporation is on the quantity of liquid diverted around the tunnel.

414 Fig. 8. Effect of high relative humidity on evaporation and seepage rates.

415 **ECRB Cross Drift**

416 In this subsection, two different data sets from liquid release tests conducted in borehole
417 LA2, Zone 2 and Zone 3, are compared with the ECRB Cross Drift seepage model. The liquid
418 release rate, seepage rate, and relative humidity data, as well as modeled liquid-release rates and
419 fitted seepage rates, are plotted in Fig. 9. The best-fit capillary-strength parameter $1/\alpha$ were 557
420 ± 56 Pa for zone 2 and 535 ± 58 Pa for zone 3, based on 21 and 19 inversions, respectively. Note
421 that both of the liquid-release tests were conducted concurrently. The measured and simulated
422 seepage rate fluctuations were strongly correlated to the drastic changes in relative humidity
423 (hence, evaporation). The model captured this evaporation effect satisfactorily, tracking
424 increases in measured seepage rates as relative humidity increases and vice versa.

425 Fig. 9. Calibration of seepage-rate data from liquid-release tests conducted in the ECRB Cross
426 Drift. Calculated seepage rate curves show only one of the multiple inversions.

427 The interplay between relative humidity fluctuation and dynamics of flow and ceiling
428 wetness at different times during the test in Zone 2 are visualized in Fig. 10. During this test, the
429 liquid release rate was relatively stable (steadily increasing from 31 mL/min on Day 0 to 34
430 mL/min on Day 34). However, the relative humidity fluctuated between 30% and 90% during
431 this period. Fig. 10 shows snapshots of the liquid saturation distribution on Days 0, 10, 20, and
432 30. Just before the test began, the drift wall has dried out because of the low relative humidity in
433 the drift. The liquid saturation at this time was in equilibrium was the assumed background
434 percolation flux of 2 mm/yr. On day 10 day of injection (relative humidity $\sim 70\%$), water
435 reached the crown of the drift, seepage has started, water was being diverted around the drift, and

436 wet plume has reached approximately to the elevation of the spring line. After 20 days, however,
437 the plume has shrunk significantly because of reduced humidity (approximately 12%) and
438 increased evaporation. Moreover, the seepage rate and seepage locations (indicated by inverted
439 triangles) have decreased. Before the 30-day time mark, the relative humidity rose up to
440 approximately 80%; thus, the evaporation rate was reduced, the wet plume grew, and seepage
441 rate and number of seeps increased. In general, despite the high liquid release rate, the flow
442 regime remained unsaturated. The liquid saturation was highest near the drift crown, which
443 induces a capillary pressure gradient that promoted flow diversion around the drift (capillary
444 barrier effect). Seepage and evaporation removed water from the formation as water flows
445 around the drift, limiting the spread of the wetted region on the drift wall.

446 Fig. 10. Liquid saturation distribution simulated with model calibrated against seepage-rate data
447 from liquid-release tests conducted in the Cross Drift borehole LA#2, Zone 2 at 0, 10,
448 20, and 30 days after the start of the liquid release tests. Note the correlation of tunnel
449 wall wetness to tunnel relative humidity.

450 SUMMARY AND CONCLUSIONS

451 In this paper, we (1) estimated the evaporative boundary-layer thickness by calibrating a
452 semi-physical evaporation model, which considers isothermal vapor diffusion; (2) calibrated a
453 heterogeneous fracture-continuum model against seepage-rate data; and (3) tested the effect of
454 evaporation on seepage predictions. The major conclusions of this study are listed below:

- 455 1. The simplified vapor-diffusion approach of modeling evaporation was found to be effective
456 in capturing the roles of the important environmental conditions that affect evaporation –
457 namely, relative humidity, temperature, and ventilation. Calibrated thicknesses of the

458 evaporation boundary layer were obtained for three ventilation conditions representing the
459 conditions at the liquid-release test sites at Yucca Mountain.

460 2. We found that evaporation reduces seepage significantly in tests conducted under
461 ventilated conditions. Therefore, it is important to account for evaporation effects when
462 calibrating a seepage process model against liquid-release-test data collected under
463 ventilated conditions. In contrast, the impact of evaporation on seepage rate was minimal in
464 closed-off niches, where relative humidity values were generally high. Thus, when using
465 data obtained from closed-off and/or artificially humidified niches, ignoring the effect of
466 evaporation is expected to introduce little error in the estimation of seepage-relevant
467 parameters.

468 3. The classification of ventilation regimes is based on crude assessment of the tunnel
469 environment. Bearing of external wind velocity variations (note that the Cross Drift is
470 connected to the air outside the ESF) was not accounted for. The matching between
471 measured evaporation rate and model predictions can be improved if accurate measurement
472 of air velocity in the tunnels was made.

473 **ACKNOWLEDGMENT**

474 We thank Jens Birkholzer and Guomin Li for their thorough reviews and insightful
475 comments. This work was supported by the Director, Office of Civilian Radioactive Waste
476 Management, U.S. Department of Energy, through Memorandum Purchase Order
477 EA9013MC5X between Bechtel SAIC Company, LLC, and the Ernest Orlando Lawrence
478 Berkeley National Laboratory (Berkeley Lab). The support is provided to Berkeley Lab through
479 the U.S. Department of Energy Contract No. DE-AC03-76SF00098.

480

481

482

REFERENCES

- 482
483 Bear, J., 1972. Dynamics of fluids in porous media Elsevier, New York, New York.
- 484 Birkholzer, J., G.M. Li, C.F. Tsang, and Y. Tsang, 1999. Modeling studies and analysis of
485 seepage into drifts at Yucca Mountain. *Journal of Contaminant Hydrology* 38:349-384.
- 486 Bodvarsson, G.S., W. Boyle, R. Patterson, and D. Williams, 1999. Overview of scientific
487 investigations at Yucca Mountain - the potential repository for high-level nuclear waste.
488 *Journal of Contaminant Hydrology* 38:3-24.
- 489 Deutsch, C.V., and A.G. Journel, 1992. *Gslib: Geostatistical software library and user's guide*
490 Oxford University Press, New York, New York.
- 491 Finsterle, S. 1999. Itough2 user's guide Report No. LBNL-40040. Lawrence Berkeley National
492 Laboratory.
- 493 Finsterle, S., 2000. Using the continuum approach to model unsaturated flow in fractured rock.
494 *Water Resources Research* 36:2055-2066.
- 495 Finsterle, S., and R.C. Trautz, 2001. Numerical modeling of seepage into underground openings.
496 *Mining Engineering* 53:52-56.
- 497 Finsterle, S., C.F. Ahlers, R.C. Trautz, and P.J. Cook, 2003. Inverse and predictive modeling of
498 seepage into underground openings. *Journal of Contaminant Hydrology* 62-63:89-109.
- 499 Fujimaki, H., and M. Inoue, 2003. A transient evaporation method for determining soil hydraulic
500 properties at low pressure. *Vadose Zone J* 2:400-408.
- 501 Ho, C.K., 1997. Evaporation of pendant water droplets in fractures. *Water Resources Research*
502 33:2665-2671.
- 503 Knight, J.H., J.R. Philip, and R.T. Waechter, 1989. The seepage exclusion problem for spherical
504 cavities. *Water Resources Research* 25:29-37.

- 505 LeCain, G.D. 1995. Pneumatic testing in 45-degree-inclined boreholes in ash-flow tuff near
506 superior, arizona Water-Resources Investigations Report 95-4073. U.S. Geological Survey,
507 Denver, Colorado.
- 508 Li, G.M., and C.-F. Tsang, 2003. Seepage into drifts with mechanical degradation. *Journal of*
509 *Contaminant Hydrology* 62:157-172.
- 510 Murray, F.W., 1966. On the computation of saturation vapor pressure. *J. Appl. Meteor.* 6:204.
- 511 Or, D., and T.A. Ghezzehei, 2000. Dripping into subterranean cavities from unsaturated fractures
512 under evaporative conditions. *Water Resources Research* 36:381-393.
- 513 Philip, J.R., 1989a. Asymptotic solutions of the seepage exclusion problem for elliptic-
514 cylindrical, spheroidal, and strip-shaped and disc- shaped cavities. *Water Resources*
515 *Research* 25:1531-1540.
- 516 Philip, J.R., 1989b. The seepage exclusion problem for sloping cylindrical cavities. *Water*
517 *Resources Research* 25:1447-1448.
- 518 Philip, J.R., J.H. Knight, and R.T. Waechter, 1989a. The seepage exclusion problem for
519 parabolic and paraboloidal cavities. *Water Resources Research* 25:605-618.
- 520 Philip, J.R., J.H. Knight, and R.T. Waechter, 1989b. Unsaturated seepage and subterranean holes
521 - conspectus, and exclusion problem for circular cylindrical cavities. *Water Resources*
522 *Research* 25:16-28.
- 523 Pruess, K., C. Oldenburg, and G. Moridis. 1999. Tough2 user's guide, version 2.0 LBNL-43134.
524 Lawrence Berkeley National Laboratory, Berkeley, Calif.
- 525 Rohsenow, W.M., and H. Choi, 1961. *Heat, mass and momentum transfer* Prentice-Hall Inc.,
526 Englewood Cliffs, New Jersey.
- 527 Trautz, R.C., and J.S.Y. Wang, 2001. Evaluation of seepage into an underground opening using
528 small- scale field experiments, yucca mountain, nevada. *Mining Engineering* 53:41-44.

- 529 Trautz, R.C., and J.S.Y. Wang, 2002. Seepage into an underground opening constructed in
530 unsaturated fractured rock under evaporative conditions. *Water Resources Research*
531 38:1188.
- 532 van Genuchten, M.T., 1980. A closed-form equation for predicting the hydraulic conductivity of
533 unsaturated soils. *Soil Science Society of America Journal* 44:892-898.
- 534 Wang, J.S.Y., R.C. Trautz, P.J. Cook, S. Finsterle, A.L. James, and J. Birkholzer, 1999. Field
535 tests and model analyses of seepage into drift. *Journal of Contaminant Hydrology* 38:323-
536 347.
- 537 Zhang, J.T., and B.X. Wang, 2002. Effect of capillarity at liquid-vapor interface on phase change
538 without surfactant. *International Journal of Heat & Mass Transfer* 45:2689-2694.
- 539 Zhang, J.T., B.X. Wang, and X.F. Peng, 2001. Thermodynamic aspect of the shift of concave
540 liquid-vapor interfacial phase equilibrium temperature and its effect on bubble formation.
541 *International Journal of Heat and Mass Transfer* 44:1681-1686.
542

Figures

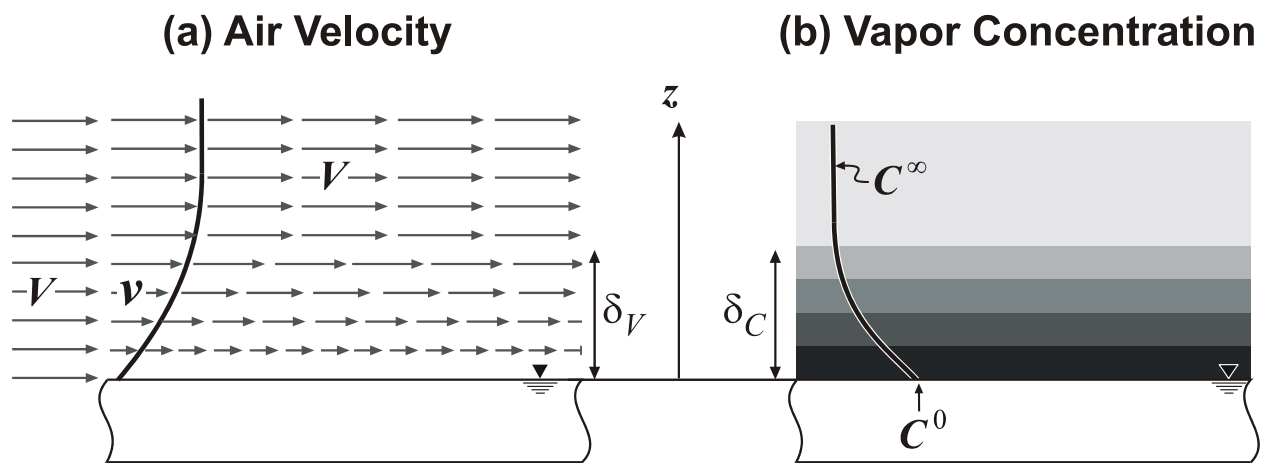


Fig. 1. Schematic description of (a) air velocity and (b) vapor concentration profiles above a free water surface

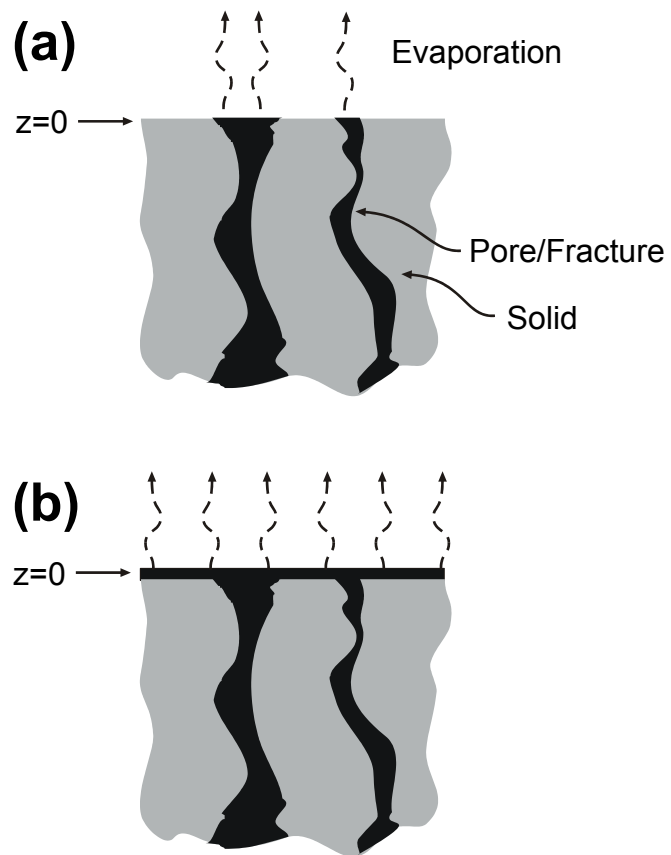


Fig. 2. Evaporating surface area of a porous medium: (a) partitioning of the surface into non-evaporating solid and evaporating pores; (b) proposed approach of uniform gas-phase surface.

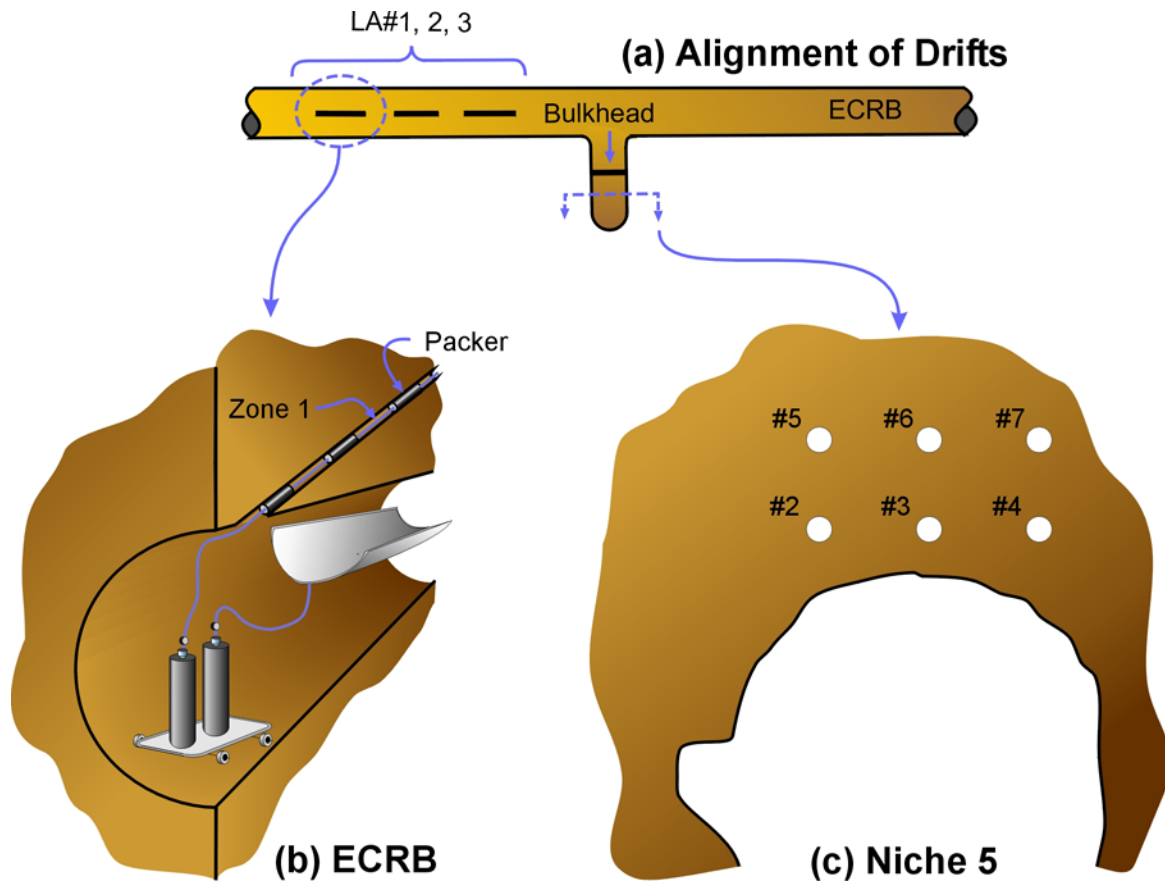


Fig. 3. Schematic alignment of tunnels and boreholes: (a) parts of the Exploratory Studies Facility (ESF) tunnel and Enhanced Characterization of the Repository Block (ECRB) cross-drift; (b) liquid release test setup in the Cross Drift, including liquid release intervals and liquid injection and seepage collection equipment; and (c) vertical section of Niche 5 along with location of all the test boreholes.

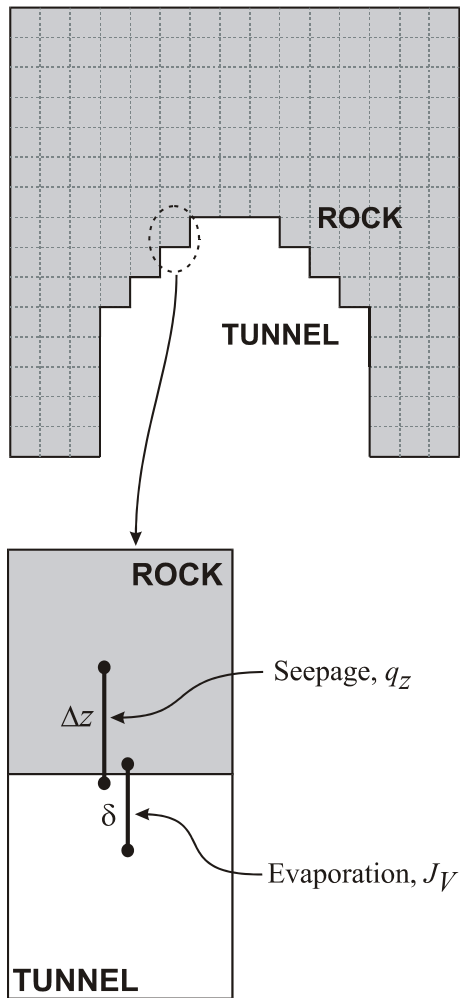


Fig. 4. Schematic description of the seepage and evaporation connections between nodes that represent the rock of the tunnel wall and the tunnel.

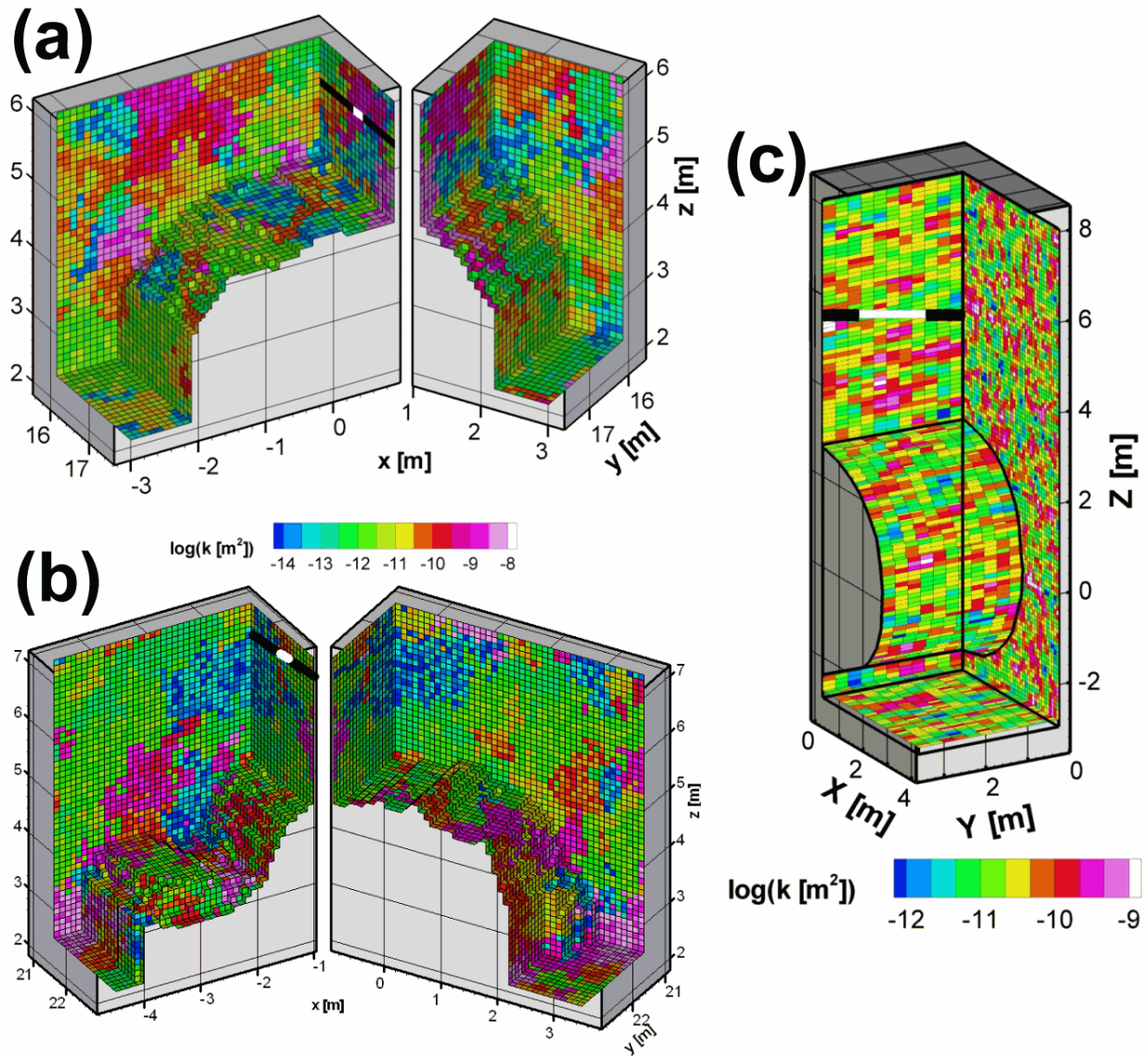


Fig. 5. Numerical meshes of (a) Niche 5 with borehole #4, (b) Niche 5 with borehole #5, and (c) the Cross Drift, along with a typical realization of the correlated stochastic permeability field. Bold black lines denote the liquid-release boreholes, and the white section in the middle of the boreholes is the injection interval.

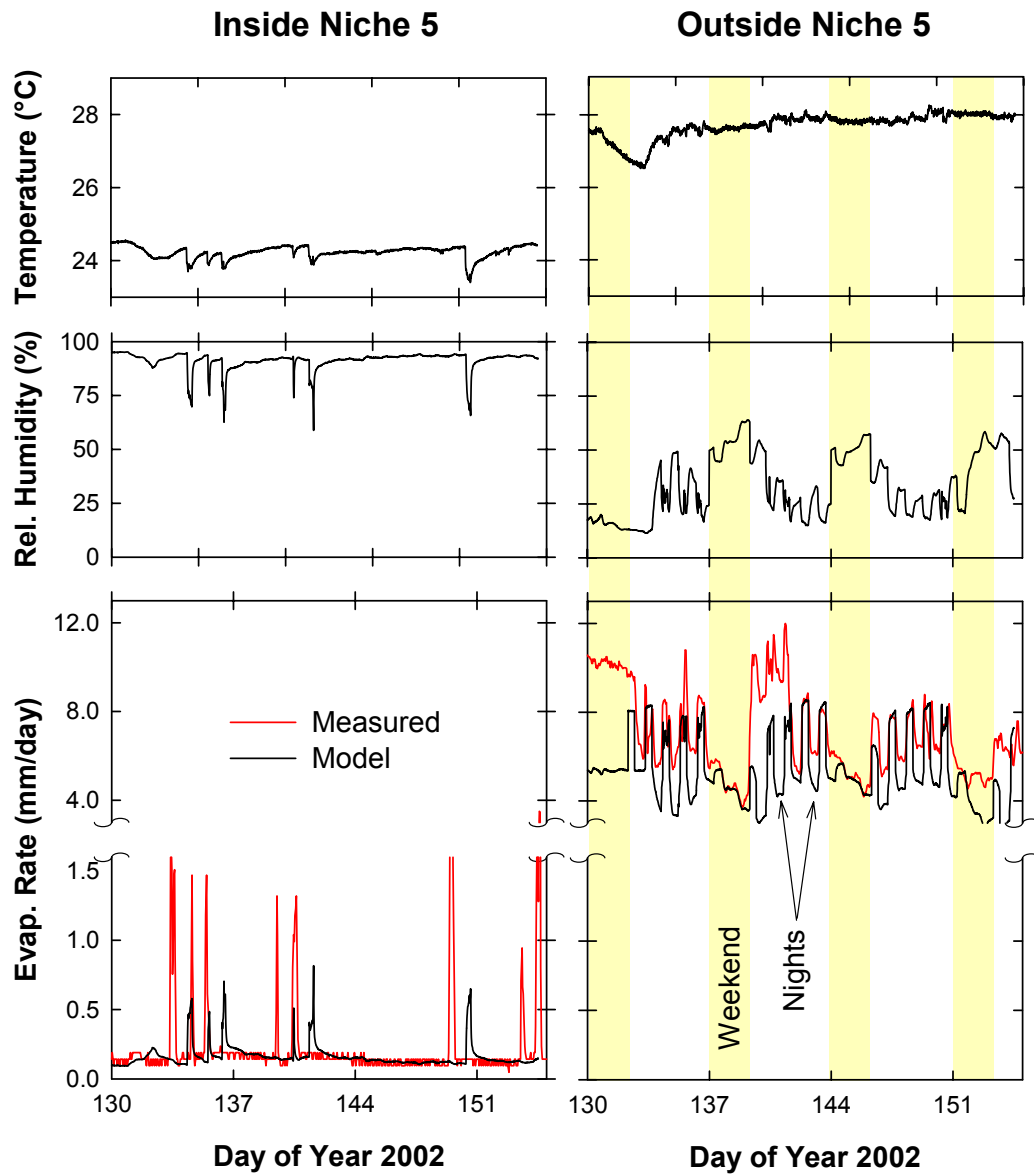


Fig. 6. Temperature, humidity, and evaporation rate data, along with model fit of the evaporation data

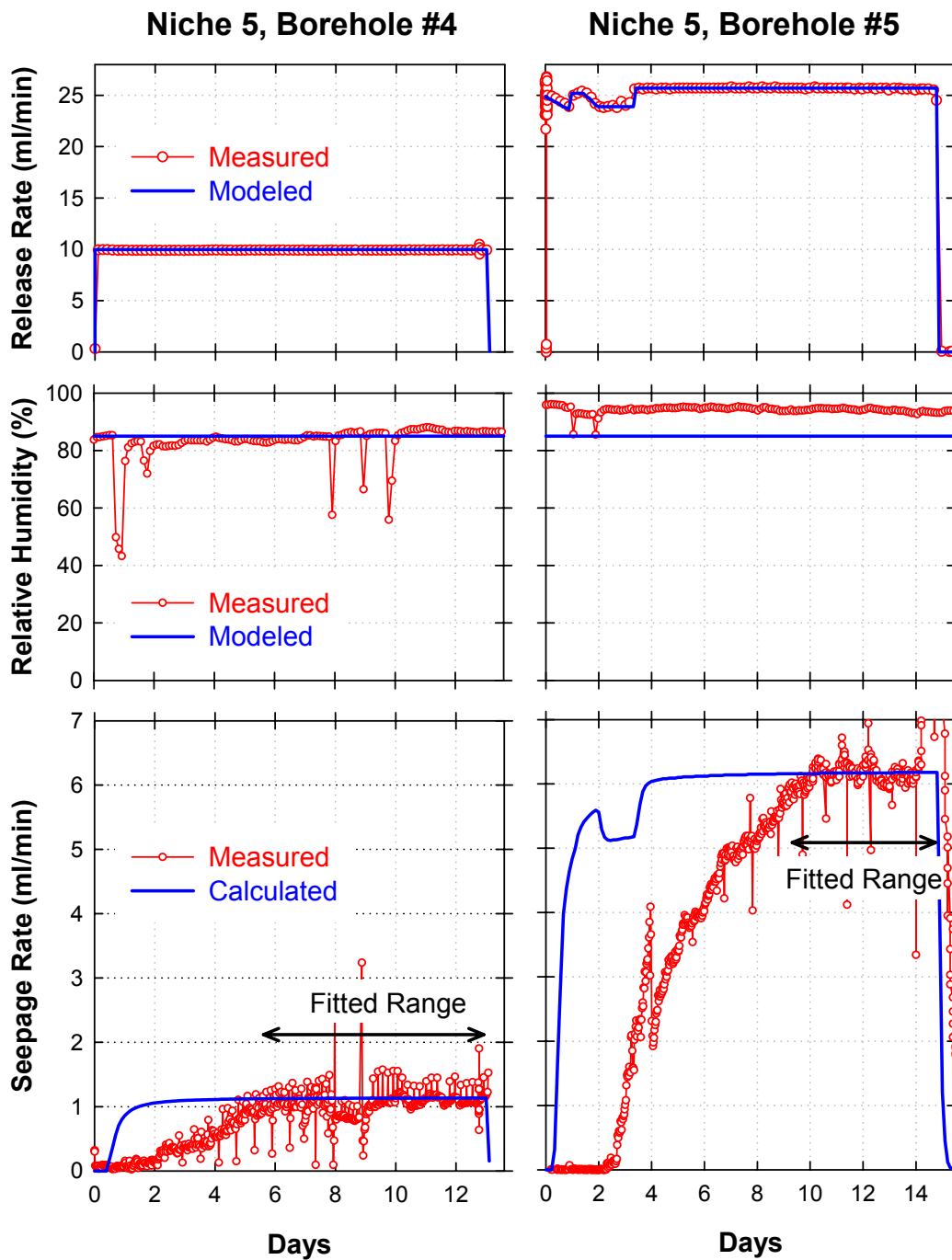


Fig. 7. Calibration of seepage-rate data from liquid-release tests conducted in Niche 5. Calculated seepage rate curves show only one of the multiple inversions.

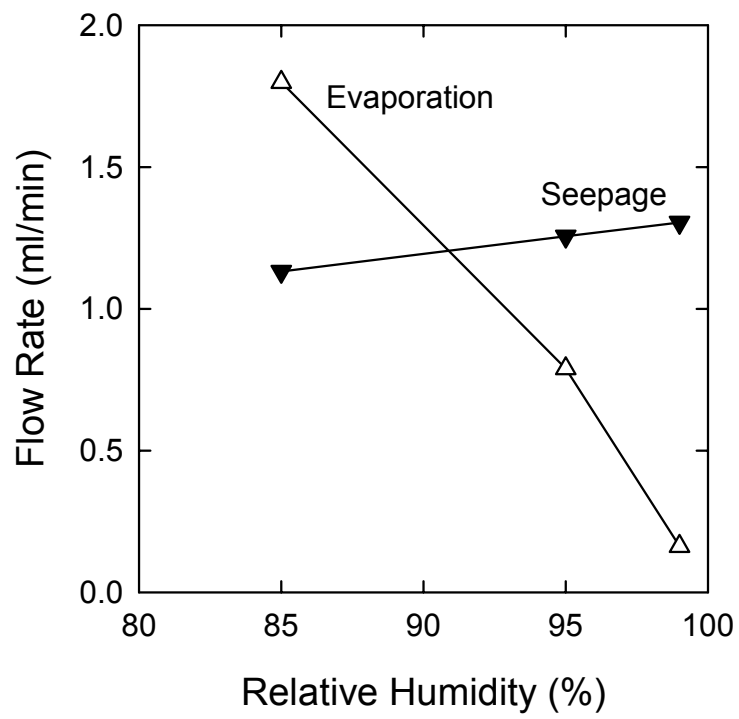


Fig. 8. Effect of high relative humidity on evaporation and seepage rates.

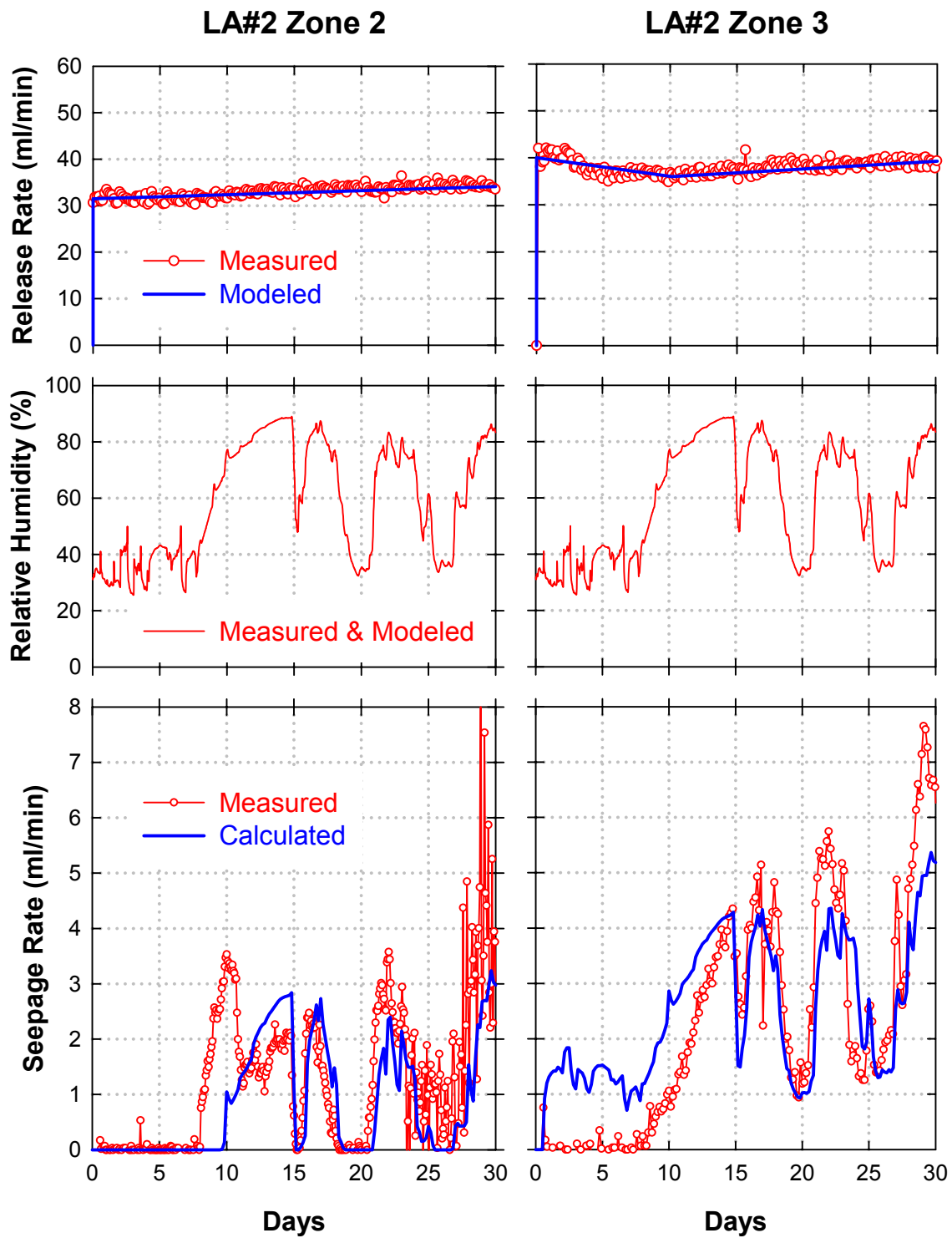


Fig. 9. Calibration of seepage-rate data from liquid-release tests conducted in the ECRB Cross Drift. Calculated seepage rate curves show only one of the multiple inversions.

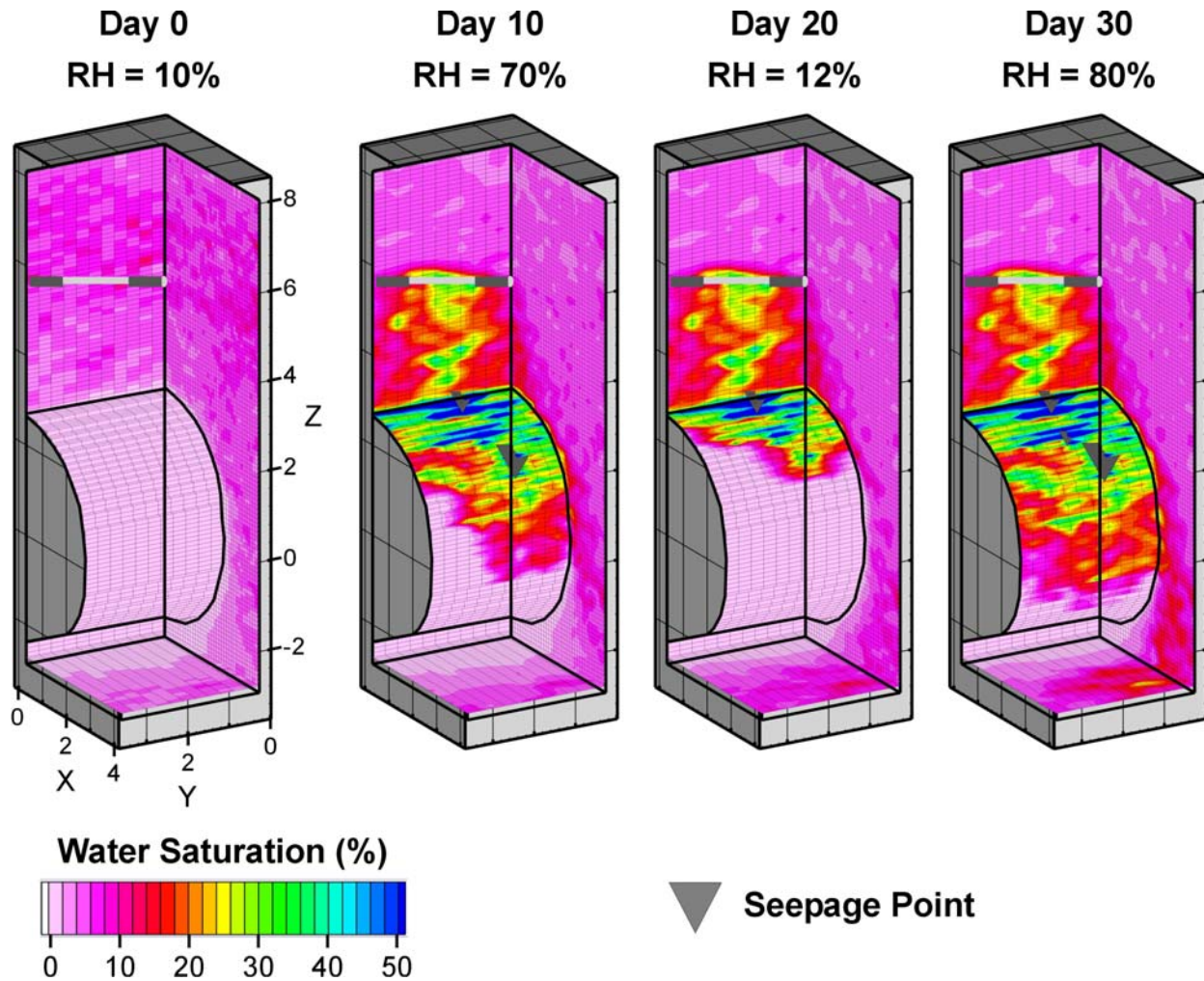


Fig. 10. Liquid saturation distribution simulated with model calibrated against seepage-rate data from liquid-release tests conducted in the Cross Drift borehole LA#2, Zone 2 at 0, 10, 20, and 30 days after the start of the liquid release tests. Note the correlation of tunnel wall wetness to tunnel relative humidity.